

Cite this: *J. Mater. Chem. A*, 2017, 5, 19714

# Vanadium nitride encapsulated carbon fibre networks with furrowed porous surfaces for ultrafast asymmetric supercapacitors with robust cycle life†

Geon-Hyoung An,<sup>a</sup> Do-Young Lee<sup>b</sup> and Hyo-Jin Ahn<sup>\*ab</sup>

Transition metal nitrides have received significant attention in view of their application as pseudocapacitive electrodes in high performance supercapacitors owing to their high capacitance, excellent electrical conductivity, high electrochemical selectivity, and low environmental impact. Nevertheless, the utilization of transition metal nitrides still encounters serious challenges due to the chemical instability of these materials during cycling in the presence of oxygen and/or water containing electrolytes, which leads to rapid capacitance fading. Here, we propose a novel structure comprising vanadium nitride encapsulated carbon fibre networks with furrowed porous surfaces prepared by electrospinning followed by an optimal stabilization and carbonization treatments. The resultant electrode shows a high energy density of 53.1–36.0 W h kg<sup>-1</sup> at high power densities in the range from 2700–54 000 W kg<sup>-1</sup>. This performance is superior to previously reported results on other asymmetric supercapacitors. Moreover, an excellent cycling stability of 92.9% at a current density of 80 A g<sup>-1</sup> after 10 000 cycles, and a superb electrode flexibility have been recorded. Our original synthesis strategy provides a useful methodology to increase the chemical stability of vanadium nitride by carbon encapsulation, which also leads to shorter diffusion pathways due to the furrowed porous surfaces and the advanced network structure consisting of 1-dimensional fibres.

Received 20th July 2017  
Accepted 30th August 2017

DOI: 10.1039/c7ta06345h

rsc.li/materials-a

## 1. Introduction

The depletion of fossil fuels and increasing environmental pollution have greatly stimulated the search for renewable and clean energy sources such as wind power, solar energy, and geothermal energy. However, the intermittent nature of energy conversion in renewable energy sources means that these cannot be directly used in electrical power grids, which demand a high power transient energy input. In this regard, due to their high power density, long cycle life, fast charging and discharging ability, wide range of operating temperatures, and safe operation, supercapacitors can function as efficient energy storage devices to provide transient energy while using renewable energy sources.<sup>1,2</sup> Supercapacitors can be typically categorized into electrical double-layer capacitors (EDLCs) and pseudocapacitors.<sup>3,4</sup> In view of their high power densities, simple components, and easy energy storage mechanism,

EDLCs have been widely used in commercial super capacitor applications. However, a crucial limitation of EDLCs is in their lower energy densities, which are of the order of 5–15 W h kg<sup>-1</sup>, principally due to the capacitive (non-faradaic) processes taking place on the carbon-based electrode material.<sup>5</sup> In contrast, pseudocapacitors can acquire higher energy densities than EDLCs by using faradaic processes occurring at the pseudocapacitive electrode, leading to higher charge storage.<sup>5</sup> Thus, pseudocapacitors (called supercapacitors in this study) consisting of an anode, cathode, electrolyte, and separator, are expected to fill in as next-generation high power energy storage devices. However, the relatively low capacitance of the anode material, which is typically made from activated carbon, is the main limitation to its wider use in different applications.

In recent times, much effort has been dedicated to improving the electrochemical performance of the anode by using pseudocapacitors based on metal oxides such as iron oxide, molybdenum trioxide, and bismuth oxide.<sup>6</sup> Nonetheless, the low electrical conductivity of these oxides leads to poor rate performance and lower power densities, when compared to EDLCs. In this context, transition metal nitrides such as vanadium nitride (VN), titanium nitride, and tungsten nitride have been investigated as alternative anode materials to overcome the limitation of metal oxides.<sup>7–9</sup> Among the potential transition

<sup>a</sup>Program of Materials Science & Engineering, Convergence Institute of Biomedical Engineering and Biomaterials, Seoul National University of Science and Technology, Seoul 01811, Korea. E-mail: hjahn@seoultech.ac.kr

<sup>b</sup>Department of Materials Science and Engineering, Seoul National University of Science and Technology, Seoul 01811, Korea

† Electronic supplementary information (ESI) available. See DOI: 10.1039/c7ta06345h

metal nitrides, VN is among the most suitable candidates due to its high specific capacitance and excellent electrical conductivity ( $1.6 \times 10^6 \Omega^{-1} \text{ m}^{-1}$ ), in addition to having an appropriate negative potential working window.<sup>10–14</sup> Despite these advantages, the VN electrode still exhibited a low electrochemical performance and showed low specific capacitance and rate performance arising from its chemical instability during cycling in oxygen and/or water containing electrolytes, which led to rapid electrochemical performance fading.<sup>15–17</sup>

Herein, we propose a novel VN encapsulated carbon fibre networks (VN/CF) structure, where the carbon fibre has a furrowed porous surface. The carbon-encapsulated VN structure, which could impede the direct contact between the VN nanoparticles and oxygen and/or water containing electrolytes, prevents the oxidation of VN during cycling, thereby leading to a robust cycle life with high specific capacitance. In addition, the focus of this work is to obtain high energy densities at high power densities, which is key to extending the application of supercapacitors to electric vehicles and electric underground locomotives. Currently, commercial supercapacitors have relatively low power densities ( $\sim 10\,000 \text{ W kg}^{-1}$ )<sup>2,3</sup> and hence, the challenging problem of developing ultrafast supercapacitors with high power densities ( $>50\,000 \text{ W kg}^{-1}$ ) is an important research topic. A powerful solution to enabling high power densities is the reduction of the ion diffusion pathway between the electrode and electrolyte by using porous electrode materials.<sup>18–20</sup> With this aim, we have designed furrowed porous surfaces on carbon fibres to provide alternative shorter ion diffusion pathways during the cycling. Thus, the novel architecture of VN/CF has two major advantages in combining a carbon-encapsulated VN structure for high specific capacitance with excellent cycling stability, with a furrowed porous surface on the carbon fibre to enable ultrafast performance.

## 2. Results and discussion

To prepare the novel VN/CF structure, we used electrospinning followed by specific stabilization and carbonization procedures, as illustrated in Fig. 1. First, the as-spun fibre (Fig. 1a) composed of VO(acac)<sub>2</sub> and PAN was prepared using electrospinning. To obtain a furrowed surface with a high number of

electrochemically active sites at high current densities, the VO(acac)<sub>2</sub>-PAN fibre was stabilized by annealing at 180 °C for 12 h in air (referred to as “stabilized fibre”), due to contraction resulting from dehydrogenation (Fig. 1b). Finally, the VN/CF (Fig. 1c) with furrowed porous surfaces was synthesized by carbonization at 800 °C for 2 h in nitrogen atmosphere.

The morphologies of the composite fibres were determined from scanning electron microscopy (SEM) analysis. Fig. 2 presents low-magnification (a–c) and high-magnification (d–f) SEM images of as-spun fibres, stabilized fibre, and VN/CF, respectively. All the samples show 1D networks; earlier studies have shown that such networks significantly increase Li-ion diffusion rate and lead to effective electron transfer, which are important targets for high performance ECs.<sup>21–23</sup> In addition, an electrode with a network structure can be ideally used in flexible and wearable energy storage devices. The as-spun fibres (Fig. 2a and d) display even surfaces, whereas stabilized fibres (Fig. 2b and e) show furrowed surfaces due to the dehydrogenation of both VO(acac)<sub>2</sub> and PAN, leading to shrinking of the fibre. In other words, the fibres contract after the stabilization treatment, leading to furrowed surfaces. Lastly, VN/CF (Fig. 2c and f) shows a furrowed porous surface, resembling a porous walnut. The observed morphology change in the VN/CF can be explained to be due to Ostwald ripening process with coarsening and recrystallization of VN nanoparticles of during carbonization, leading to grain growth of encapsulated VN nanoparticles in the carbon fibre.<sup>24</sup> Therefore, VN/CF was prepared using a controlled stabilization and carbonization procedure under specific conditions, as described in Fig. 2g.

To examine the structural features of VN/CF in greater detail, transmission electron microscopy (TEM) analysis was carried

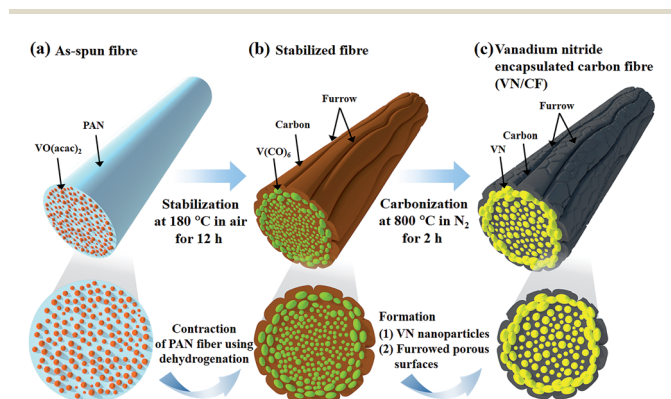


Fig. 1 Schematic illustration of the synthesis procedures for (a) as-spun fibre, (b) stabilized fibre, and (c) VN/CF.

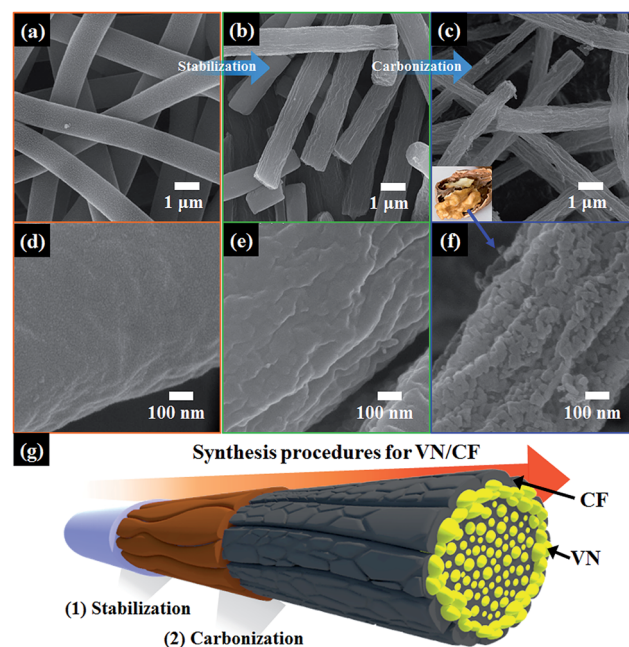


Fig. 2 (a–c) Low-magnification and (d–f) high-magnification SEM images of as-spun fibres, stabilized fibres, and VN/CF. (g) Synthesis procedures for VN/CF.

out. In the low magnification TEM image shown in Fig. 3a, dark lines are seen on the VN/CF sample, indicating a furrowed porous surface. In addition, VN nanoparticles (35–41 nm in size) are totally encapsulated in the carbon fibre, as shown in Fig. 3b. The continuous carbon layer of thickness  $\sim 5.3$  nm on the VN nanoparticle was investigated using high magnification TEM (Fig. 3c). A lattice spacing of 0.23 nm corresponding to the (111) plane of VN was measured from Fig. 3d.<sup>25</sup> To confirm the distribution of vanadium, nitrogen, and carbon contents in VN/CF, TEM energy dispersive X-ray (EDX) analysis was performed, as displayed in Fig. 3e. The EDX data demonstrate that the different elements are well dispersed, proving that VN nanoparticles are all encapsulated in the carbon fibre; thus, the carbon fibre efficiently encapsulated VN nanoparticles. The carbon-encapsulated VN nanoparticles are expected to strongly resist oxidation during the cycling, leading to high capacitance with robust cycle life. In addition, the furrowed porous surfaces on the thin carbon coating can reduce the diffusion length between VN and the electrolyte, leading to higher electrochemically active sites at high current densities.

Fig. 4a displays the X-ray diffraction (XRD) patterns of the as-spun fibre, stabilized fibre, and VN/CF. The as-spun fibre shows a diffraction peak at  $13.1^\circ$ , corresponding to the (002) plane of  $V(C_5H_7O_2)_3$  with an orthorhombic structure. The stabilized fibre shows a diffraction peak at  $16.8^\circ$ , corresponding to the (210) plane of  $V(CO)_6$  with orthorhombic structure, and a broad peak around  $25^\circ$ , corresponding to the (002) plane of graphite.<sup>26</sup> Thus,  $V(C_5H_7O_2)_3$  was transformed to  $V(CO)_6$  during the stabilization process through the reaction  $4V(C_5H_7O_2)_3 + 39O_2 = 4V(CO)_6 + 42H_2O + 36CO$ . This reaction generated the furrowed surfaces, resulting from the dehydrogenation of  $V(C_5H_7O_2)_3$ . VN/CF also shows a broad peak around  $25^\circ$ , corresponding to the (002) plane of graphite, and diffraction peaks at  $37.6^\circ$  and  $43.7^\circ$ , corresponding to the (111) and (200) planes of VN with a face centred structure. These results support the conclusion that the VN phase was successfully obtained along with a carbon phase during the carbonisation process according to

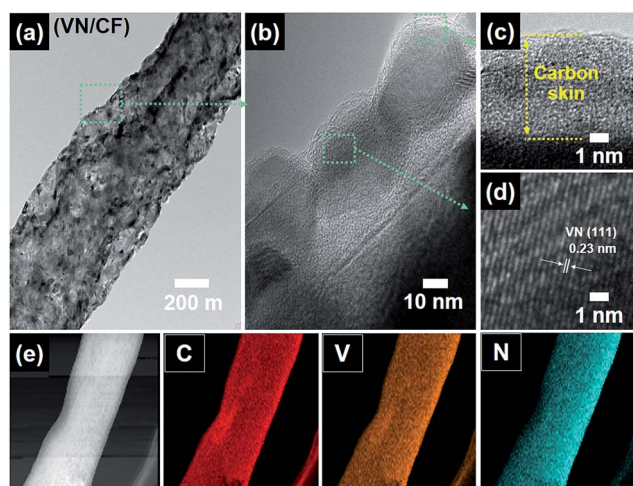


Fig. 3 (a) Low-magnification and (b–d) high-magnification TEM images of VN/CF. (e) TEM-EDX spectrum of VN/CF.

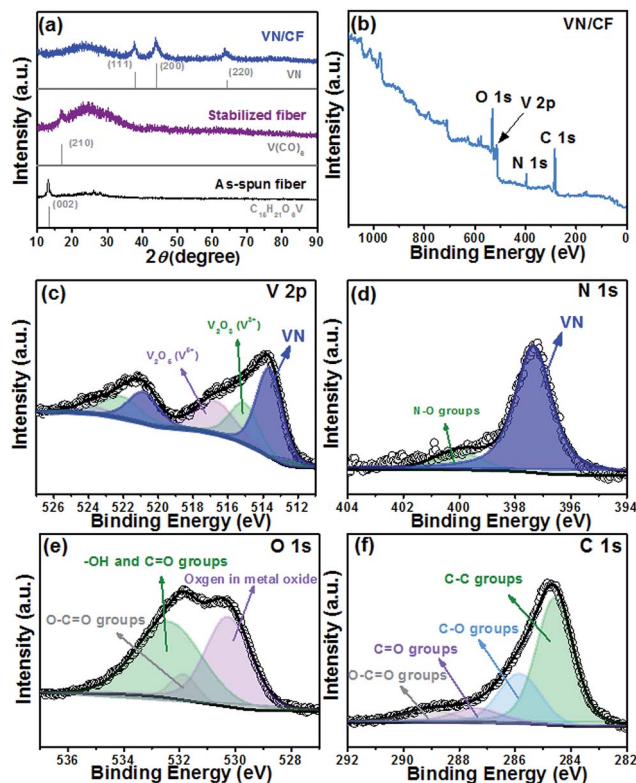


Fig. 4 (a) XRD patterns of as-spun fibres, stabilized fibres, and VN/CF. (b) XPS full scan spectrum of VN/CF. XPS spectra of (c) V 2p, (d) N 1s, (e) O 1s, and (f) C 1s of VN/CF.

the reaction  $V(CO)_6 + N = VN + 6CO$ . The N atoms of VN were originated from PAN during a carbonization process, as shown in the Fig. S1.† In addition, the content of VN nanoparticles in VN/CF was investigated by thermal gravimetric analysis (TGA) measurement from 50 to  $800^\circ C$  at a heating rate of  $10^\circ C \text{ min}^{-1}$  in air, as presented in Fig. S2.† VN/CF indicated weight losses of 42%, implying the existence of VN nanoparticles in CFs. Also, the specific surface area of VN/CF indicates  $271 \text{ m}^2 \text{ g}^{-1}$ , as shown in Fig. S3.† Fig. 4b shows the X-ray photoelectron spectroscopy (XPS) full scan spectrum of VN/CF consisting of O 1s, V 2p, N 1s and C 1s peaks, confirming the presence of O, V, N, and C elements with no other impurity phase. It is well known that the surface of VN is easily oxidized to  $V_2O_5$ , with a higher oxidation state, as shown in Fig. S4.† Nevertheless, V 2p spectrum of VN/CF (Fig. 4c) presents a typical signal at  $\sim 513.7 \text{ eV}$ , corresponding to the VN phase, implying successful carbon-encapsulation of VN.<sup>13,14,27</sup> Other low intensity signals at  $\sim 515.2 \text{ eV}$  and  $\sim 517.0 \text{ eV}$  correspond to the different valence states ( $V^{3+}$  and  $V^{5+}$ ) of  $V_2O_3$ , and  $V_2O_5$ .<sup>28</sup> The N 1s XPS spectrum of VN/CF (Fig. 4d) showed two signals at  $\sim 397.3 \text{ eV}$  and  $\sim 399.9 \text{ eV}$ , corresponding to the VN and N–O groups, respectively. The V/N atomic ratio is determined to be 1.03, which is close to the stoichiometric value for VN having the face centred cubic structure.<sup>29</sup> Fig. 4e displays the O 1s spectrum VN/CF. The signals obtained at  $\sim 530.2 \text{ eV}$ ,  $\sim 531.8 \text{ eV}$ , and  $\sim 532.3 \text{ eV}$ , correspond, respectively, to oxygen in vanadium oxide, –OH groups, and O–C=O groups.<sup>13,14,27,30</sup> In addition, the C 1s

spectral peaks of VN/CF (Fig. 4f) can be de-convoluted into four signals peaking at 284.5, 286.1, 287.5, and 288.7 eV, corresponding to C–C groups, C–O groups, C=O groups, and O–C=O groups, respectively.<sup>28</sup> These results reveal successful carbon-encapsulation of VN, which is in accordance with the high magnification TEM results.

To elucidate the formation mechanism of VN/CF, the as-spun fibre was stabilized at 150, 180, and 200 °C in air for 12 h and then carbonized in an equivalent condition, as illustrated in Fig. 5a. The stabilized fibre at 150 °C (Fig. S5a and c†) shows an even surface without the porous structure due to the fact that the treatment temperature was too low to cause fibre contraction. When stabilised at 180 °C, VN/CF with a furrowed porous surface was selectively obtained. However, at 200 °C, the morphology of as-spun fibre is visibly changed to form a nanorod like structure (Fig. S5b and d†) owing to greater grain growth at higher temperatures. In addition, XRD analysis of this sample shows the crystal structure to be that of V<sub>2</sub>O<sub>3</sub> (Fig. S6†). Thus, to clarify the phase-change behaviour, the vanadium precursor VO(acac)<sub>2</sub> was studied using differential scanning calorimetry (DSC) analysis in the temperature range 50–550 °C under air, as displayed in Fig. 5b. An exothermic peak starts at 200 °C, corresponding to an oxidative process, which indicates that VO(acac)<sub>2</sub> is oxidized to V<sub>2</sub>O<sub>3</sub> at 200 °C during the stabilization process, as illustrated in Fig. 5c. Also, the V<sub>2</sub>O<sub>3</sub> phase is maintained after carbonization because of its highly stable oxidation state. Thus, an optimized stabilization temperature is required to form novel VN phases as well obtain morphology control to form furrowed porous surfaces.

Fig. 6a and b illustrate the electrochemical reactions  $\text{VN}_x\text{O}_y + \text{OH}^- \leftrightarrow \text{VN}_x\text{O}_y/\text{OH}^- + \text{VN}_x\text{O}_y\text{-OH}$  using commercial VN and

VN/CF. The real specific capacitance of commercial VN is very low, which means that VN can be easily oxidized in oxygen and/or water, blocking further electrochemical reactions of VN, as indicated in Fig. 6a. To resolve this problem, it is necessary to passivate the surface of VN using a protecting layer. Hence, we introduced a carbon fibre coating to prevent the oxidation of VN, as illustrated in Fig. 6b. Moreover, the furrowed porous surfaces prepared using the specific stabilization treatment improved electrochemical performance due to the higher number of electrochemically active sites and a shorter diffusion length between VN and electrolyte at high current densities. To understand the dependence of the electrochemical behaviour on capacitive energy storage, the galvanostatic charge–discharge curves and cyclic voltammetry (CV) were carried out in 6.0 M KOH aqueous solution in the potential range –1.2 to 0.0 V. For comparison, fibres stabilized at 150 °C and 200 °C were also tested (referred to as S-150 and S-200, respectively). Fig. 6c presents the galvanostatic charge–discharge curves for commercial VN, VN/CF, S-150, and S-200 at 4 A g<sup>-1</sup>. It is clear that commercial VN shows the shortest charge–discharge time compared to the other samples due to the formation of an oxide layer on the surface, as shown in Fig. S4b.† In contrast, VN/CF shows the longest charge–discharge time compared to the other samples, signifying a larger charge storage. The symmetric triangle shape and linear slopes of VN/CF imply a predominantly capacitive behaviour. In addition, there is no marked voltage drop, which also reveals the excellent capacitive characteristic of VN/CF. Fig. 6d shows the specific capacitances at the current density of 4–80 A g<sup>-1</sup> for the different samples. The specific capacitances of commercial VN, VN/CF, S-150, and S-200 at the current density of 4 A g<sup>-1</sup> are 43, 800, 530, and 14 F g<sup>-1</sup>, respectively. Remarkably, VN/CF exhibits the highest specific capacitance as compared to the other samples at all current densities. S-150 has a low capacitance due to a smooth surface with smaller number of electroactive sites on the surface. S-200 also shows a low specific capacitance, which means that the V<sub>2</sub>O<sub>3</sub> phase has no electrochemical reactions in the potential range –1.2 to 0.0 V. When the current density is increased, the related specific capacitance decreases slightly because of the rapid ion diffusion during the charging and discharging process. Nevertheless, VN/CF displays excellent capacitance retention of 73%, whereas, S-150 shows a low capacitance retention of 37% due to its even surface with a longer ion diffusion pathway. Therefore, the impressive specific capacitance and high capacitance retention of VN/CF is mainly ascribed to two reasons. First, VN with a unique structure was completely acquired with a few oxidation layers on the surface, leading to the high specific capacitance. Secondly, the furrowed porous surfaces with thin carbon skin could efficiently provide a shorter ion diffusion pathway, leading to excellent capacitance retention. Fig. 6e shows the CV curves of VN/CF at scan rates from 10 to 200 mV s<sup>-1</sup> in the potential range of –1.2 to 0.0 V, illustrating the typical behaviour of VN.<sup>13,14</sup> The redox reactions were monitored at potentials ranging from –0.8 to –0.5 V and –0.7 to –0.9 V, to elucidate the capacitive mechanism in VN/CF consisting of faradaic reactions. In addition, it can be clearly seen that the curves maintained their original

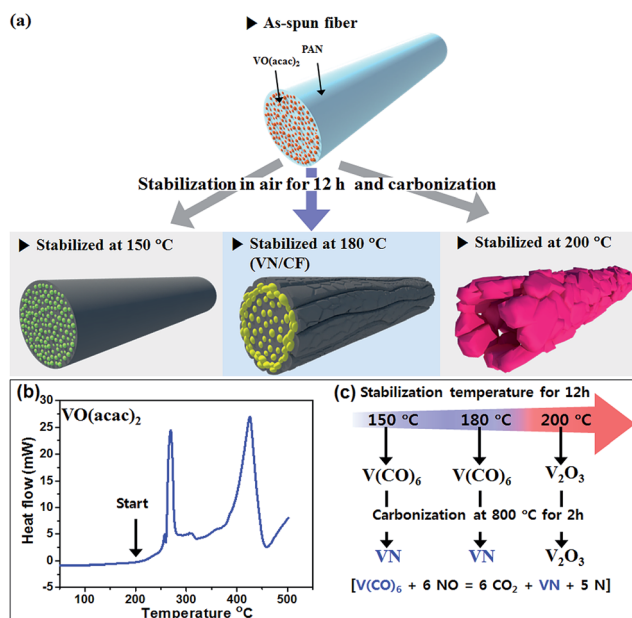


Fig. 5 (a) Schematic illustration of the formation mechanism during stabilization at 150, 180, 200 °C. (b) DSC analysis of VO(acac)<sub>2</sub> in the temperature range 50–550 °C under air. (c) Phase transitions from V(CO)<sub>6</sub> to VN or V<sub>2</sub>O<sub>3</sub> during the stabilization process.

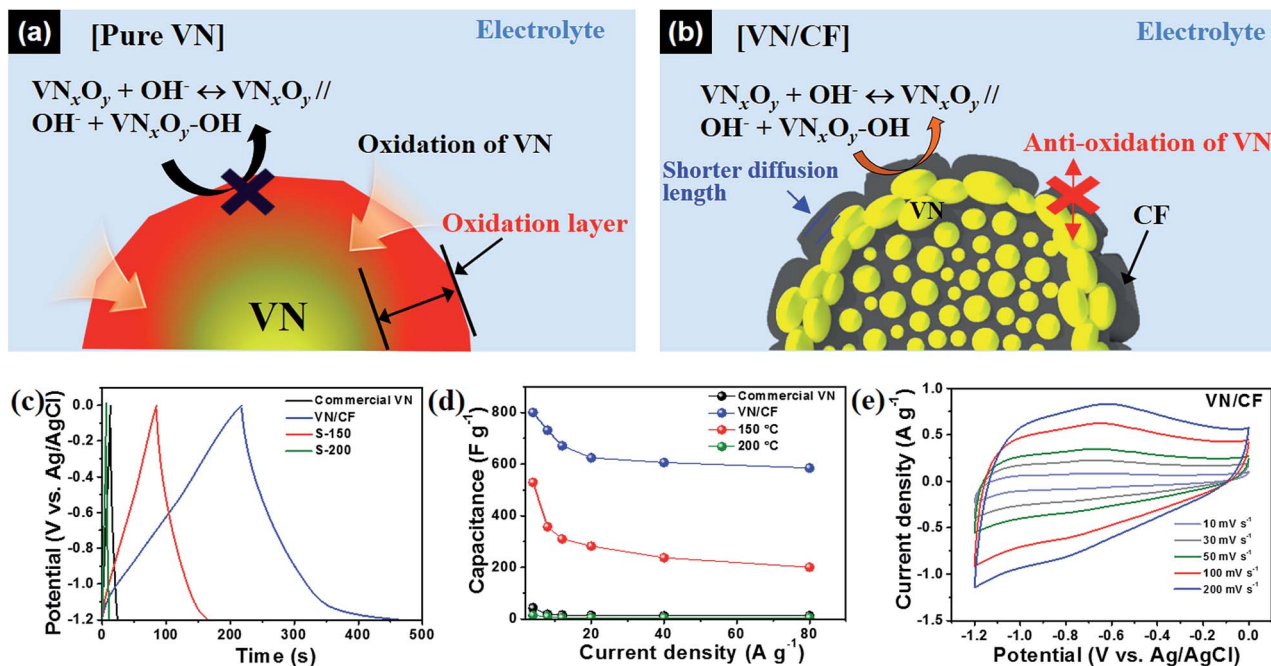


Fig. 6 Illustration of electrochemical reactions  $\text{VN}_x\text{O}_y + \text{OH}^- \leftrightarrow \text{VN}_x\text{O}_y/\text{OH}^- + \text{VN}_x\text{O}_y\text{-OH}$  for (a) a commercial VN and (b) VN/CF. (c) Galvanostatic charge–discharge curves and (d) calculated specific capacitance of commercial VN, VN/CF, S-150, and S-200 at current densities in the range 4–80  $\text{A g}^{-1}$  in the potential range –1.2 to 0.0 V. (e) CV curves of commercial VN, VN/CF, S-150, and S-200 at scan rates varying from 10 to 200  $\text{mV s}^{-1}$  in the potential range –1.2 to 0.0 V.

shapes even at increased current densities implying an ideal faradaic reaction.

To further investigate VN/CF for practical application in energy storage devices, an asymmetric supercapacitor was constructed using VN/CF as the anode,  $\text{Ni}(\text{OH})_2$  as the cathode, and 6 M KOH as the electrolyte, as illustrated in Fig. 7a. CV curves (Fig. 7b) with the couple of redox reactions in the potential range 0.0 to 1.6 V show similar capacitive responses when scanned at different rates from 10 to 200  $\text{mV s}^{-1}$ , implying pseudo-capacitive behaviour between the VN/CF and  $\text{Ni}(\text{OH})_2$  electrodes in the electrolyte. The galvanostatic charge–discharge curves at different current densities from 4–80  $\text{A g}^{-1}$  are displayed in Fig. 7c. The galvanostatic charge–discharge curves at all the current densities show nearly symmetric behaviour, signifying excellent reversibility. In addition, the specific capacitance is calculated to be 188  $\text{g}^{-1}$  from the galvanostatic charge–discharge curves at a current density of 4  $\text{A g}^{-1}$ , which is much higher than previously reported results for VN electrodes in supercapacitor applications.<sup>13,14,31</sup> The energy and power densities are important parameters used in practical evaluation of supercapacitors for application in energy storage. From the specific capacitance values, the energy density and power density are obtained as described in the Ragone plot (Fig. 7d). An energy density of 53.1  $\text{W h kg}^{-1}$  is acquired at a power density of 2700  $\text{W kg}^{-1}$ . Moreover, the energy density of 36.0  $\text{W h kg}^{-1}$  is still obtained at a high power density of 54 000  $\text{W kg}^{-1}$ . Thus it is clear that our supercapacitor shows much higher energy and power densities when compared to previously reported results from asymmetric supercapacitors, which are summarized in Table S1.<sup>†</sup> Thus, the

application VN/CF-based supercapacitor can potentially expand to areas of energy storage at high power densities (referred to as ultrafast supercapacitor). Moreover, the cycling stability at high energy densities is key to using this capacitor in practical applications. Fig. 7e displays the cycling stability of the prepared supercapacitor at varying current densities of 4, 40, and 80  $\text{A g}^{-1}$  (2700, 27 000, and 54 000  $\text{W kg}^{-1}$ ) over 10 000 cycles. Remarkably, our supercapacitor shows an excellent cycling stability with a superb capacitance retention of 96.4, 95.3, and 92.9% at current densities of 4, 40, and 80  $\text{A g}^{-1}$ , respectively, even after 10 000 cycles. These results are attributed to the excellent electrochemical stability of VN/CF, which means that carbon-encapsulated VN could strongly resist oxidation and structural breakdown. After 10 000 cycles at a current density of 80  $\text{A g}^{-1}$ , VN shows no chemical and structural changes, as described in Fig. S7 and S8.<sup>†</sup>

Pliable electrode materials to fabricate flexible supercapacitors have recently attracted much attention due to their potential use as energy and power sources in wearable electronics such as smart clothing, fashion electronics, and distributed sensors. Thus, the electrochemical performances of the highly flexible VN/CF electrode were tested using a straight electrode (Fig. 8a) and a bent electrode (Fig. 8b) in KOH electrolyte. The galvanostatic charge–discharge curves were measured at a current density of 4  $\text{A g}^{-1}$ , and the results are shown in Fig. 8c. Similar curves are obtained with identical charge–discharge time and redox behaviour even when the electrode was bent by 180°, indicating that the network structure-based VN/CF electrode retains excellent mechanical stability and shows high flexibility. In addition, the cycling

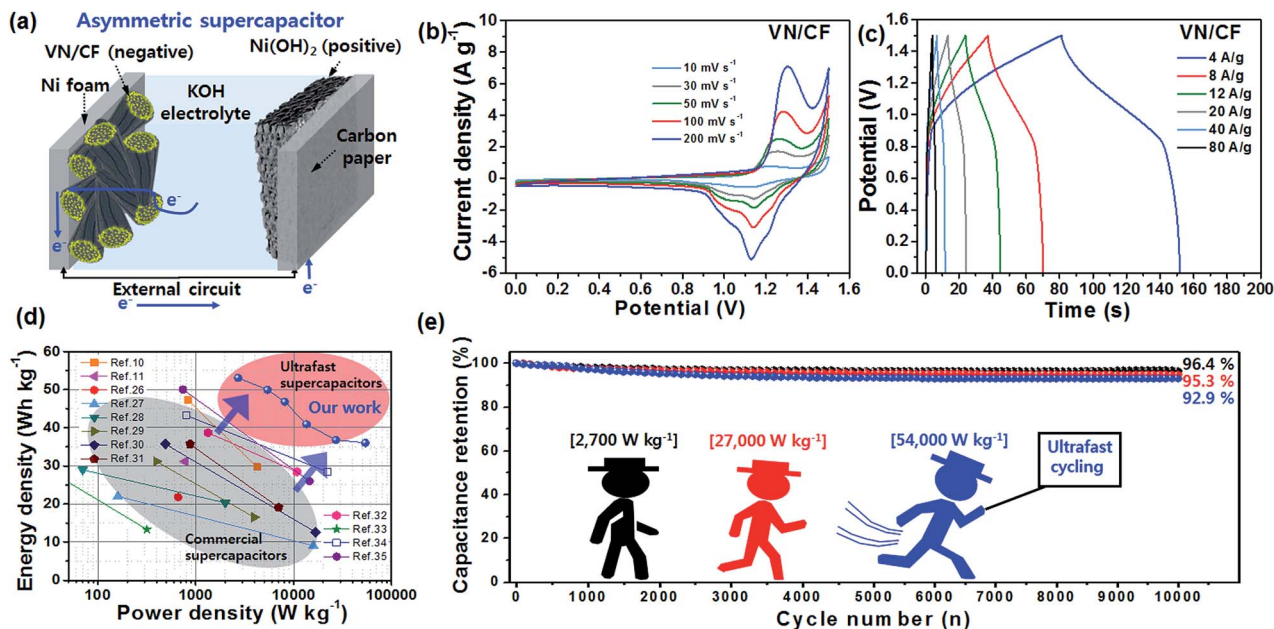


Fig. 7 (a) Illustration of an asymmetric supercapacitor assembled using VN/CF as the negative electrode, Ni(OH)<sub>2</sub> as the positive electrode, and 6 M KOH electrolyte. (b) CV curves at different scan rates ranging from 10 to 200 mV s<sup>-1</sup> in the potential range of 0.0 to 1.6 V. (c) Galvanostatic charge–discharge curves at current densities from 4–80 A g<sup>-1</sup> in the potential range of 0.0 to 1.6 V. (d) Ragone plots related to energy and power densities for a comparison with previously reported results on supercapacitors. (e) Cycling stability at different current densities of 4, 40, and 80 A g<sup>-1</sup> (2700, 27 000, and 54 000 W kg<sup>-1</sup>) over 10 000 cycles.

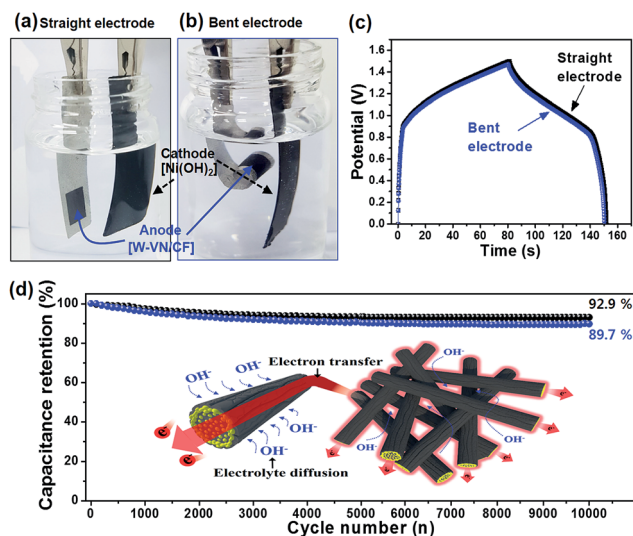


Fig. 8 Preparation of the VN/CF electrode for bending test using (a) straight and (b) bent electrodes. (c) Galvanostatic charge–discharge curves at the current density of 4 A g<sup>-1</sup> in the potential range of 0.0 to 1.6 V using straight and bent electrodes. (d) Cycling stability at the current density of 80 A g<sup>-1</sup> (54 000 W kg<sup>-1</sup>) over 10 000 cycles using straight and electrodes.

stability of the flexible supercapacitor is important for practical applications. Thus, cycling tests were carried out at a high current density of 80 A g<sup>-1</sup> over 10 000 cycles; the results are shown in Fig. 8d. Remarkably, the bent electrode shows excellent capacitance retention of 89.7% after 10 000 cycles, demonstrating the superb flexibility resulting from the

extended network structure. Furthermore, VN/CF electrode with the gel-type electrolyte consisting of polyvinyl alcohol and KOH for solid-state supercapacitor showed outstanding flexibility, as shown in Fig. S9.†

Thus, we have achieved remarkable electrochemical performance for a supercapacitor by designing a novel structure. This increased performance can be explained to be due to several effects. First, the unique VN phase with high capacitance and excellent electrical conductivity provides significantly higher energy densities. Secondly, the furrowed porous surface of VN/CF enables a shorter ion diffusion pathway, leading to ultrafast performance at high power densities. Thirdly, the carbon-encapsulation can effectively prevent oxidation of VN during cycling, leading to a robust cycle life. Lastly, the advanced network structure-based VN/CF offers a good mechanical stability, leading to excellent flexibility.

### 3. Conclusions

VN/CF was successfully synthesized using electrospinning followed by a specific stabilization and a carbonization procedure. By optimizing the stabilization conditions, we obtained a novel morphology for carbon-encapsulated VN nanoparticles in carbon fibre with furrowed porous surfaces as well as the formation of an extended 1D network. Thus, VN/CF electrode, when incorporated in a full cell, showed a remarkable electrochemical performance, with a high energy density of 53.1–36.0 W h kg<sup>-1</sup> at the high power densities in the range 2700–54 000 W kg<sup>-1</sup>. These values are superior to previously reported results on other asymmetric supercapacitors. An excellent

cycling stability of 92.9% at a current density of 80 A g<sup>-1</sup> after 10 000 cycles in addition to superb flexibility, was observed for our samples. The remarkable electrochemical characteristics are attributed to four main factors: (i) the high energy density is due to the unique VN phase; (ii) a high power density is achieved due to the furrowed porous surfaces; (iii) the impressive ultrafast cycling stability is intimately related to carbon-encapsulated VN nanoparticles; and (iv) the outstanding flexibility is attributed to the advanced network structure. Therefore, this work demonstrates that VN/CF has great potential as an electrode in supercapacitors and also provides new insights into the ultrafast electrochemical performance of transition-metal nitrides.

## Conflicts of interest

There are no conflicts to declare.

## Acknowledgements

This research was supported by Basic Science Research Program through the National Research Foundation of Korea (NRF) funded by the Ministry of Science, ICT and Future Planning (NRF-2015R1A1A1A05001252).

## References

- 1 P. Simon, Y. Gogotsi and B. Dunn, *Science*, 2014, **343**, 1210–1211.
- 2 P. Simon and Y. Gogotsi, *Nat. Mater.*, 2008, **7**, 845–854.
- 3 G. Wang, L. Zhang and J. Zhang, *Chem. Soc. Rev.*, 2012, **41**, 797–828.
- 4 S. Dong, X. Chen, L. Gu, X. Zhou, L. Li, Z. Liu, P. Han, H. Xu, J. Yao, H. Wang, X. Zhang, C. Shang, G. Cui and L. Chen, *Energy Environ. Sci.*, 2011, **4**, 3502–3508.
- 5 Z. Yu, L. Tetard, L. Zhai and J. Thomas, *Energy Environ. Sci.*, 2015, **8**, 702–730.
- 6 M. Yu, Z. Wang, Y. Han, Y. Tong, X. Lu and S. Yang, *J. Mater. Chem. A*, 2016, **4**, 4634–4658.
- 7 M. Balogun, W. Qiu, W. Wang, P. Fang, X. Lu and Y. Tong, *J. Mater. Chem. A*, 2015, **3**, 1364–1387.
- 8 S. Dong, X. Chen, X. Zhang and G. Cui, *Coord. Chem. Rev.*, 2013, **257**, 1946–1956.
- 9 X. Zhang, X. Chen, K. Zhang, S. Pang, X. Zhou, H. Xu, S. Dong, P. Han, Z. Zhang, C. Zhang and G. Cui, *J. Mater. Chem. A*, 2013, **1**, 3340–3346.
- 10 Y. Yan, B. Li, W. Guo, H. Pang and H. Xue, *J. Power Sources*, 2016, **329**, 148–169.
- 11 B. Gao, X. Li, X. Guo, X. Zhang, X. Peng, L. Wang, J. Fu, P. K. Chu and K. Huo, *Adv. Mater. Interfaces*, 2015, **2**, 1500211.
- 12 J. Balamurugan, G. Karthikeyan, T. D. Thanh, N. H. Kim and J. H. Lee, *J. Power Sources*, 2016, **308**, 149–157.
- 13 Y. Yang, L. Zhao, K. Shen, Y. Liu, X. Zhao, Y. Wu, Y. Wang and F. Ran, *J. Power Sources*, 2016, **333**, 61–71.
- 14 Y. Wu and F. Ran, *J. Power Sources*, 2016, **344**, 1–10.
- 15 P. J. Hanumantha, M. K. Datt, K. Kadakia, C. Okoli, P. Patel and P. N. Kumta, *Electrochim. Acta*, 2016, **207**, 37–47.
- 16 Y. Xu, J. Wang, L. Shen, H. Dou and X. Zhang, *Electrochim. Acta*, 2015, **173**, 680–686.
- 17 L. Zhang, C. M. B. Holt, E. J. Luber, B. C. Olsen, H. Wang, M. Danaie, X. Cui, X. Tan, V. W. Lui, W. P. Kalisvaart and D. Mitlin, *J. Phys. Chem. C*, 2011, **115**, 24381–24393.
- 18 G. H. An, B. R. Koo and H. J. Ahn, *Phys. Chem. Chem. Phys.*, 2016, **18**, 6587–6594.
- 19 G. H. An, H. J. Ahn and W. K. Hong, *J. Power Sources*, 2015, **274**, 536–541.
- 20 G. H. An and H. J. Ahn, *Carbon*, 2013, **65**, 87–96.
- 21 B. Zhao, S. Jiang, C. Su, R. Cai, R. Ran, M. O. Tadeb and Z. Shao, *J. Mater. Chem. A*, 2013, **1**, 12310–12320.
- 22 G. H. An, D. Y. Lee and H. J. Ahn, *ACS Appl. Mater. Interfaces*, 2017, **9**, 12478–12485.
- 23 G. H. An, D. Y. Lee, Y. J. Lee and H. J. Ahn, *ACS Appl. Mater. Interfaces*, 2016, **8**, 30264–30270.
- 24 Y. Song, T. Liu, B. Yao, M. Li, T. Kou, Z.-H. Huang, D.-Y. Feng, F. Wang, Y. Tong, X.-X. Liu and Y. Li, *ACS Energy Lett.*, 2017, **2**, 1752–1759.
- 25 X. Lu, M. Yu, T. Zhai, G. Wang, S. Xie, T. Liu, C. Liang, Y. Tong and Y. Li, *Nano Lett.*, 2013, **13**, 2628–2633.
- 26 G. H. An, D. Y. Lee and H. J. Ahn, *J. Alloys Compd.*, 2017, **722**, 60–68.
- 27 T. Rostamzadeh, S. Adireddy, X. Zhang, B. Koplitz, D. B. Chrisey and J. B. Wiley, *ChemNanoMat*, 2016, **2**, 54–60.
- 28 G. H. An, D. Y. Lee and H. J. Ahn, *ACS Appl. Mater. Interfaces*, 2016, **8**, 19466–19474.
- 29 C. M. Ghimbeu, E. Raymundo-Pinero, P. Fioux, F. Beguin and C. Vix-Guterl, *J. Mater. Chem.*, 2011, **21**, 13268–13275.
- 30 Y. Z. Su, K. Xiao, N. Li, Z. Q. Liu and S. Z. Qiao, *J. Mater. Chem. A*, 2014, **2**, 13845–13853.
- 31 R. Wang, X. Yan, J. Lang, Z. Zheng and P. Zhang, *J. Mater. Chem. A*, 2014, **2**, 12724–12732.
- 32 Q. T. Qu, Y. Shi, L. L. Li, W. L. Guo, Y. P. Wu, H. P. Zhang, S. Y. Guan and R. Holze, *Electrochem. Commun.*, 2009, **11**, 1325–1328.
- 33 K. Xu, R. Zou, W. Li, Q. Liu, X. Liu, L. An and J. Hu, *J. Mater. Chem. A*, 2014, **2**, 10090–10097.
- 34 H. B. Li, M. H. Yu, F. X. Wang, P. Liu, Y. Liang, J. Xiao, C. X. Wang, Y. X. Tong and G. W. Yang, *Nat. Commun.*, 2013, **4**, 1894.
- 35 J. Zhang, J. P. Cheng, M. Li, L. Liu, F. Liu and X. B. Zhang, *J. Electroanal. Chem.*, 2015, **743**, 38–45.
- 36 F. Lu, M. Zhou, W. Li, Q. Weng, C. Li, Y. Xue, X. Jiang, X. Zeng, Y. Bando and D. Golberg, *Nano Energy*, 2016, **26**, 313–323.
- 37 Y. S. I. Zhitomirsky, *J. Power Sources*, 2014, **7**, 235–242.
- 38 J. Yang, C. Yu, X. Fan, S. Liang, S. Li, H. Huang, Z. Ling, C. Hao and J. Qiu, *Energy Environ. Sci.*, 2016, **9**, 1299–1307.
- 39 S. Y. Kim, H. M. Jeong, J. H. Kwon, I. W. Ock, W. H. Suh, G. D. Stucky and J. K. Kang, *Energy Environ. Sci.*, 2015, **8**, 188–194.